The continuous melting process in a cloud-scale model using a bin microphysics scheme

Céline Planche, Wolfram Wobrock, Andrea Flossmann

To cite this version:

Céline Planche, Wolfram Wobrock, Andrea Flossmann. The continuous melting process in a cloud-scale model using a bin microphysics scheme. Quarterly Journal of the Royal Meteorological Society, 2013, 140 (683), pp.1986 - 1996. 10.1002/qj.2265 . hal-01893484

HAL Id: hal-01893484
https://uca.hal.science/hal-01893484v1

Submitted on 31 Oct 2021

The continuous melting process in a cloud scale model using a bin microphysics scheme

Céline Planche [a,b,c], Wolfram Wobrock [a,b], Andrea I. Flossmann [a,b]

[a] Clermont Université, Université Blaise Pascal, Laboratoire de Météorologie Physique, F-63000 Clermont-Ferrand, France

[b] CNRS, INSU, UMR 6016, LaMP, F-63171 Aubière, France

[c] Present address: Institute for Climate and Atmospheric Science, School of Earth and Environment, University of Leeds, Leeds, UK

Manuscript submitted to

Quarterly Journal of the Royal Meteorological Society

1 February 2013

Revised on 11th September 2013

Accepted for publication on 26th September 2013

<u>Corresponding author address:</u>

Dr. Céline Planche

School of Earth and Environment

ICAS, University of Leeds

Leeds, LS2 9JT, UK

Email: C.Planche@leeds.ac.uk

Tel/Fax: +44(0) 113 34 36473/35259

Abstract

Simulations of an idealised stratiform cloud system are performed with the 3D cloud scale model DESCAM-3D (DEtailed SCAvenging Model) using a bin resolved microphysics scheme for ice, water and aerosol particles. This idealised case corresponds to numerical simulations of moist airflow over a narrow isolated mountain and a gentle slope in order to obtain a stratiform situation where radar bright band phenomena are often visible. For this dynamical situation the impact of a detailed time-dependent melting scheme has been studied. This scheme allows the calculation of a water/ice ratio within each mass bin for the melting ice crystals. The results obtained with this detailed melting process are compared with corresponding results from simulations involving instantaneous melting at the 0ºC isotherm level. The new detailed melting scheme allows a penetration of the ice phase in the positive temperature areas. Most of the mass of falling ice particles melts over a distance of a few hundred meters. The non-instantaneous melting scheme also produces a deeper layer of latent cooling that slightly modified the dynamical field.

With the detailed melting scheme, a simple backscattering scheme is implemented in order to consider the wetted ice particles and simulate the bright band phenomenon. It supposes that the backscattering proportions of the wetted ice particles are similar to those of raindrops. The association of the non-instantaneous melting process with this backscattering scheme permits to reproduce the radar bright band phenomenon. This study will enable a better understanding of the complex microphysics inside the melting layer and then will help to reduce the radar uncertainties in the precipitation estimation at the ground.

Keywords: Ice melting, mixed phase hydrometeor, detailed microphysics, radar bright band.

1. Introduction

In stratiform precipitating systems, the radar echoes often show a region of increased reflectivity in the layer where ice particles are melting. This region called “bright band” is triggered when ice particles acquire dielectric properties more similar to those of drops. Since the beginning of quantitative radar measurements, the bright band has been considered as a source of error in precipitation estimates, and the need to remove its effects has been recognized repeatedly (Smith, 1986; Klaassen, 1988; Joss and Waldvogel, 1990; Fabry and Zawadzki, 1995; Hardaker *et al.*, 1995; Szyrmer and Zawadzki, 1999; Olson *et al.*, 2001). In fact, the melting particles influence the electromagnetic measurements (Battan, 1973) and the bright band properties depend on the precipitating particles and the microphysical processes involved in the precipitation formation (Fabry and Zawadzki, 1995).

When atmospheric ice particles fall through the 0ºC level, they start to melt. The exact temperature at which melting begins depends mainly on the humidity of the air. The melting process may extend over some distance during the fall of the ice particle, depending on the size of the particle, as well as the temperature and humidity of the air. The melting rate of ice particles in the atmosphere affects the rate at which the environmental air cools by its consumption of latent heat of melting. This cooling affects the vertical motion in the atmosphere, as well as its stability (Liu *et al.*, 1997, Phillips *et al.*, 2007). Accurate knowledge of the rate of melting of atmospheric ice particles is therefore of considerable importance for the cloud dynamics and microphysics modelling. Unfortunately, very few quantitative data has been provided by previous studies on the rate at which ice particles melt. Rasmussen and Pruppacher (1982) and Rasmussen *et al.* (1984a, b) studied the melting process of the ice particles in a wind tunnel at the micro-scale. But only numerical models are capable to generalize the findings of a detailed description of the melting layer and study their influence on the cloud level.

In the past, already modelling efforts have been made to study the impact of the melting of ice particles on the mixed-phase cloud systems. In a first approach, one-dimensional vertical simulations were made (Klaassen, 1988; Mitra *et al.*, 1990). However, the effects arising from the horizontal variability of the conditions controlling the phase change are not adequately represented in this model method. In a further approach, two- or three- dimensional dynamics models were coupled with a bulk parameterisation of the microphysics (Szeto *et al.*, 1988; Barth and Parsons, 1996; Wei and Marwitz, 1996 among others). But, in the simulation of a full particle size spectrum is computationally prohibitive. Szyrmer and Zawadzki (1999) developed a single-moment scheme simulating the melting of snow using an exponential size distribution truncated by the largest snowflakes that have completely melted when falling through the melting layer. In a two-moment approach, Thériault and Stewart (2010) assumed that the smallest snowflakes melt completely before the largest ones and based on that assumption, they considered different types of winter precipitation. Indeed, they assumed that the wet snow melts partially into slush particles (particle composed of liquid water mixed with ice whose the density is assumed the same as a raindrop) those then completely melt into rain when falling through the melting layer. The bulk schemes can also use another approach to represent a non-instantaneous melting process where the portion of the melted ice mass is shed as rain at every time step (Morrison *et al.*, 2009; Ferrier, 1994).

Due to the computational burden of 3D bin microphysics simulations, some previous bin studies have either considered an instantaneous melting scheme at the 0ºC isotherm level (Ovtchinnikov and Kogan, 2000; Fridlind *et al.*, 2004; Lynn *et al.*, 2005) or an one- or two-dimensional bin microphysics representation (Olson *et al.*, 2001; Phillips *et al.*, 2007). For example, in order to represent the melting process, the 2D scheme of Phillips *et al.* (2007) allows calculation of liquid water fraction within each mass bin of melting hydrometeors. This paper presents a first attempt to simulate in a 3D bin manner the melting of the atmospheric ice particles in order to understand this complex microphysical layer and, represent and analyse the bright band phenomenon. Nevertheless, the representation of the bright band needs both a non-instantaneous melting process and a backscattering scheme in order to, respectively, characterize the mixed-phase hydrometeors visible in this phenomena and reproduce the radar observations.

The exact calculation of backscattering of microwave radiation by melting particles is not easy due to the lack of information concerning the detailed micro-structure of in-homogeneities present in the melting particles. In this context, a variety of different methodologies have been developed that result in a large variability of the electromagnetic properties of melting particles. The most widely used formulation for the dielectric constant of the melting ice particles follows the Maxwell Garnett approach (Maxwell-Garnett, 1904) that considers randomly ice inclusions in a water matrix. Bohren and Battan (1982) generalized this approach for randomly ice elliptical inclusions in a water matrix. Meneghini and Liao (1996) assumed that the melting particles are subdivided into a grid of cells containing ice, air, or liquid water. Moreover, Fabry and Szyrmer (1999) represented melting particles using a concentric ice core and a liquid shell with different dielectric properties.

In the current study, a non-instantaneous melting process and a backscattering scheme are implemented in a three-dimensional bin microphysics model in order to reproduce the complex microphysics of the bright band phenomena. The detailed explanations of these schemes, as well as a brief description of the 3D bin microphysics model, are given in the section 2. The section 3 presents the characteristics of the idealised stratiform situation used to investigate the influence of the melting process on the mixed-phase cloud system. Section 4 shows the sensitivity studies about the role of the non-instantaneous melting process on the microphysics and thermodynamics of the cloud system, as well as, the impact of the non-instantaneous approach for the melting process to represent the bright band phenomenon. Section 5 summarizes and concludes the findings.

2. Model description

The 3D cloud model with detailed (bin) microphysics used herein couples the 3D non-hydrostatic model of Clark and Hall (1991) with the Detailed Scavenging Model DESCAM (Flossmann and Wobrock, 2010; Planche *et al.*, 2010) for the microphysical package.

The microphysical scheme follows the evolution of the aerosol and drop size density distribution. In order to follow the fate of the uptaken particles in the hydrometeors, one additional mass density distribution function calculate the aerosol mass in each size bin for the drops. In presence of ice phase, two more density distributions are considered for the number of ice crystals of mass m_i and for the aerosol particle mass in the ice crystal bin. The aerosol mass in drops and in ice crystals is followed by two distribution functions in order to close the aerosol budget. All distribution functions are divided in 39 bins and use logarithmically spaced mass coordinates with mass doubling every subsequent bin. The aerosol particles and drops range from 1 nm to 7 μm and from 1 μm to 12 mm, respectively. The coordinates for the distribution function is mass of the ice crystal instead of the radius for the drop and the aerosol particle functions, which allows more easily getting around the shape effect. The mass range of the ice phase is assumed the same than the drops distribution. In fact, the assumption of the ice density (*e.g.* 0.9 g cm^{-3}), allows passing between the drop and the ice density distribution functions without making assumptions regarding the shape of the ice particles. Work to extend the model to a size dependant ice density is under way. The warm microphysical processes considered in DESCAM-3D are aerosol particle growth and activation to drops, droplet deactivation, growth of drops by condensation and collision-coalescence, and break-up. The mathematical treatment of the different microphysical processes is summarized in Flossmann and Wobrock (2010), where the detailed references can be found.

Concerning the cold microphysics processes, DESCAM-3D describes the homogeneous and heterogeneous ice nucleation, ice growth by vapour deposition, riming and melting. The formation of ice crystals considers homogeneous nucleation according to Koop *et al.* (2000), as well as heterogeneous nucleation following Meyers *et al.* (1992). This parameterization gives only a number of activated ice nuclei at a given ice supersaturation ratio. Thus, all aerosol particles and drops, whatever their size, are assumed to nucleate with the same efficiency. Nevertheless, this ice nucleation formulation yielded the best results for cirrus clouds during the INCA campaign (Monier *et al.*, 2006). Riming of ice crystals and coalescence of droplets are treated by solving the stochastic equation of collection from Flossmann *et al.* (1985). The collection efficiencies for riming are set to be the same as those for collision–coalescence. The collection efficiency of a spherical ice crystal is assumed equal to the one of a water drop of the same diameter. Heymsfield and Pflaum (1985) have shown that the drop equivalent approach overestimates the measured collection efficiency and that the collection efficiencies are most accurately predicted by using the mixed-Froude number approach of Hall (1980) and Rassmussen and Heymsfield (1985). As this method was developed for the collection efficiencies of plate-like ice crystals, we refrained from using it as our ice particles are assumed to be spherical and prefer to stay with the drop equivalent approach. To stay consistent with this choice, the terminal velocities of spherical ice crystals are assumed the same as those for droplets with the same mass. The terminal velocities of the ice crystals are calculated thanks to the approach of Heymsfield and Iaquinta (2000).

The ice category of the DESCAM microphysical scheme used hereafter is therefore represented in a simple approach. Indeed, the ice category is represented by only one type of spherical ice species with a bulk density of 0.9 g cm^{-3} for all ice crystals, including aggregates. As the ice bulk density is fixed, no dependence on density for the ice particle fall speeds is taken into account, which will overestimate their fall speed and underestimate their melting. This ice representation implicates some limitations e.g. on the representation of the bright band phenomena which is function of both the properties of the hydrometeors and their fall speeds, but also, the characterisation of the ice species present in the melting layer (snow, aggregate, hail…). So, it is necessary to keep in mind these approximations will only provide an upper limit for the extent of the bright band in the upcoming analyses of the simulation results obtained for an idealised case.

2.1. Microphysics of the melting scheme

The new detailed melting scheme in DESCAM-3D is based on the model of Mason (1956) and on the lab experiments of Rasmussen and Pruppacher (1982) and Mitra *et al.* (1990). Melting generally starts at 0°C. However, evaporative cooling of the surface of melting ice particle falling in sub-saturated air counteracts the melting process and therefore increases the time and distance a melting ice particle must fall before it has completely melted. Thus, the onset of melting is often delayed, causing melting to begin only at temperatures considerably warmer than 0°C (see Rasmussen and Pruppacher (1982) and Pruppacher and Klett (1997)). While the surface of the ice is dry, before the onset of melting, also sublimation occurs. This sublimation causes a pronounced latent cooling. After melting has started, evaporation of meltwater occurs instead of sublimation, also causing a latent cooling.

For each environmental relative humidity RH_e, there is a critical environmental temperature $T_{e,crit}$ at which melting begins. According to Rasmussen and Pruppacher (1982), this temperature can be calculated from the Eq. (1), which is based on Mason (1956), by considering that melting begins when the surface temperature T_s of the ice crystal is equal to

0°C (named T_0). Therefore, at time t, the melting ice particle consists of a spherical ice core of radius a surrounded by a layer of water of thickness $(b - a)$ which is assumed to be uniform and concentric with the ice core. Figure 1 schematically explains the melting process at the time t and the Eq. (1) describes the melting rate of the ice particles:

$$L_m 4\pi\rho_i a^2 \frac{da}{dt} = -4k_w \pi ab \frac{\left(T_s - T_0\right)}{\left(b-a\right)} = -\left\{4\pi b k_a f_h\left(T_e - T_s\right) + L_e 4\pi b D_v f_v\left[\rho_v\left(T_e\right) - \rho_s\left(T_s\right)\right]\right\} \qquad (1)$$

where L_m is the latent heat of melting, k_w the heat of conductivity of water, ρ_i the bulk density of the ice core, k_a thermal conductivity of air, f_h and f_v are the ventilation coefficients for heat and vapour flux, respectively, L_e is the latent heat of evaporation and D_v is the diffusivity of water vapour in air. $\rho_v(T_e)$ and $\rho_v(T_s)$ are the water vapour densities far away and at the particle surface, respectively.

Equation (2) gives the critical environment of temperature at which melting begins assuming that $f_h \approx f_v$ (Pruppacher and Klett, 1997), calculated by setting the right-hand side of Eq. (1) equal to zero:

$$T_{e,crit} = T_s + \frac{D_v L_e}{k_a}[\rho_v(T_s) - \rho_v(T_e)] \qquad (2)$$

Equation (2) was experimentally verified by Rasmussen and Pruppacher (1982), showing that, with decreasing relative humidity, the onset of melting shifts to temperatures above 0°C. Figure 2 adapted from Rasmussen and Pruppacher (1982) shows the dependency of the critical environmental temperature $T_{e,crit}$ for several relative humidity as given by Eq. (2). Thus, at an atmospheric relative humidity of 60%, *e.g.*, the melting begins at +3.2°C.

The shape of the curve drawn in the Figure 2 directly provides the critical environmental temperature as a function of the relative humidity of the air (RH_e) and can be accurately represented using a fourth-order polynomial function limiting computational effort. Equation (3) $T_{e,crit} = f(RH_e)$ can be used (with RH_e in decimal e.g. 0.90 for 90% of atmospheric relative humidity) in DESCAM-3D to determine the critical environmental temperature $T_{e,crit}$ (in Kelvin) at which melting begins.

$$T_{e,crit} = 285.64 - 26.07 RH_e + 27.23 RH_e^2 - 19.86 RH_e^3 + 6.23 RH_e^4 \qquad (3)$$

Figure 2 shows in addition to the theory of Mason (1956), the experiments given by Rasmussen and Pruppacher (1982) and the parameterisation for the critical air temperature $T_{e,crit}$ at which melting begins. The critical temperatures obtained with the Eq. (3) are closed to the theoretical ones since the maximum bias is less than 0.5°C when the atmospheric relative humidity is assumed equal to 10%.

After onset of melting, time dependent melting is calculated by Eq. (1) assuming that 1‰ of the ice initial mass melted instantaneously in order to eliminate the numerical division by zero. The mass of the particle is assumed to remain the same at all time. Therefore, during the melting process, the meltwater is assumed to accumulate on the exterior of the ice particle forming a liquid layer of thickness (b – a) and the shedding process (Rasmussen and Heymsfield, 1987a) is neglected. According to Phillips *et al.* (2007), the meltwater of the ice particles with a bulk density ≥ 0.9 g cm^{-3}, as in DESCAM-3D, does not enter in the interior of the ice particle and the ice particles are not considered spongy.

The ice crystals with a size lower than 10 µm (corresponding to the 9 first bins of the ice crystal distribution) melt very quickly and have a smaller influence in the radar bright band calculation than the larger ones. So, these particles are assumed to melt instantaneously when $T_e \geq T_{e,crit}$. In order to consider the melting of the larger crystals, a distribution of the water ice ratio (WIR) of the particle is added in the model. The melted liquid water proportion in each mass bin of ice particles is advected along with the particles. When the WIR is near the unity (90%), the ice particles are transferred into the equivalent drop classes. The procedure of transferring the ice crystals into the drops classes is detailed in the Figure 3.

In order to determine the melting rate of the ice crystals, also a parameterisation of Eq. (1) based on Mason (1956) and Rasmussen and Pruppacher (1982) is developed which takes into account that the temperature and the humidity of the air mostly influence the melting process. On the other hand, the atmospheric pressure and the ice water proportion of the ice crystal have a lesser impact on the melting process. These assumptions are supported e.g. in Rasmussen and Heymsfield (1987a, b). However, as DESCAM-3D only considers one type of ice particles with a fixed density of 0.9 g cm^{-3}, the density parameter influence is not considered in this melting rate parameterisation. This assumption will have to be modified when the DESCAM model will consider different ice morphologies (or ice densities).

The parameterisation of the rate of the ice mass melting into liquid water is given by the Eq. (4). This equation uses the same derivative approach than the Eq. (1) where the left-hand side $4\pi\rho_i a^2 \frac{da}{dt}$ becomes $\frac{dm_{r,i}}{dt}$. Moreover, as described in Rasmussen and Pruppacher (1982), the theoretical approach of Mason (1956) is able to predict qualitatively the correct trend for the rate of melting with ice particle size and heating rate (*i.e.* environmental conditions such as the temperature (in Kelvin) and the humidity (in decimal)). From the lab experiments of Rasmussen and Pruppacher (1982), the dimensions of the ice core inside the melting crystal was determined as a function of time, and from latter the total melting time was found. The disagreement between the results obtained from the theoretical approach and the lab experiment was attributed to the pronounced asymmetric melting and the internal circulation in the meltwater, both of which were disregarded in Mason's theory. So, in order to consider the correction of Rasmussen and Pruppacher (1982), the Eq. (4) is function of the ice mass of the ice particle not yet melted (in grams), *i.e.* the residual ice mass $m_{r,i}$ of the particle:

$$\frac{dm_{r,i}}{dt}(T_e, RH_e, m_{r,i}) = [A(T_e)RH_e + B(T_e)]m_{r,i}^{1/3} \tag{4}$$

$A(T_e)$ and $B(T_e)$ are two third-order polynomial functions depending of the temperature T_e. They are given by the following equations:

$$A(T_e) = -0.3140 + 0.0004T_e - 1.3935\mathrm{E}^{-5}T_e^2 + 1.7952\mathrm{E}^{-8}T_e^3 \quad (5)$$

$$B(T_e) = -0.6435 + 0.0072T_e - 2.7019\mathrm{E}^{-5}T_e^2 + 3.3820\mathrm{E}^{-8}T_e^3 \quad (6)$$

Various tests on the influence of the temperature and the humidity have been performed and showed that the parameterised melting times are in average only 10% greater than the ones found by Rasmussen and Pruppacher (1982) and Rasmussen *et al.* (1984a, b). Figure 4 shows an example of comparison between the melting process observed by Rasmussen and Pruppacher (1982) and obtained with the melting rate parameterisation in different environments. The biggest difference between the theory and the parameterisation appears for the warming rate of $+3.0^{o}$C min^{-1} and corresponds to a time delay of about 5 seconds.

Adjustment of the ambient temperature and humidity is performed by the melting scheme as a result of the phase changes. The terminal fall velocity of the melting ice particles is not adjusted. Indeed, the terminal fall velocity of the wetted ice particles is closed to the rain drops velocity as the initial ice density is 0.9 g cm^{-3}. However, when in the future, DESCAM will consider different ice morphologies, this adjustment in the terminal fall velocity will be mandatory.

An aggregation process which is most efficient around 0°C, when the ice particles develop a pseudo-liquid layer (Pruppacher and Klett, 1997), was also implemented in DESCAM. Furthermore, below the melting levels, the collisions between the drops and melting ice particles are considered. Aggregation and collision between drop and wetted ice particle are treated similar to the coalescence and riming processes using also the numerical scheme of Bott (1998).

The stochastic collection equation (Pruppacher and Klett, 1997) which defines the aggregation process is given by:

$$\frac{\partial f(m_f)}{\partial t} = \frac{1}{2}\int_0^{m_f} f(m_f - m)K(m_f - m, m)f(m)dm - f(m_f)\int_{spectra} K(m_f, m)f(m)dm \tag{7}$$

where K (m_f - m, m) is the collection kernel describing the rate at which an ice particle of mass (m_f - m) = m' is aggregated by an ice particle of masse m thus forming an ice particle of mass m_f. The collection kernel which is calculated using the collection efficiencies E (m', m) of Hall (1980) is given by:

$$K(m', m) = \pi(r' + r)^2|V_\infty(r') - V_\infty(r)|E(m', m) \tag{8}$$

where r and r' are the respective radius of the ice particles falling with a terminal velocity of $V_\infty(r)$ and $V_\infty(r')$. Equation (7) represents thus the formation of an ice particle of mass m_f by aggregation between two ice particles of mass m' and m and, the possible aggregation between this new forming ice particle with the others of the ice spectra.

The collision between drop and wetted ice particle is described by a similar method, with the aggregation distribution f, by the following equations:

$$\frac{\partial f(m_{drop})}{\partial t} = -\int f_{wat}(m_{drop})K(m_{crys}, m_{drop})f_{ice}(m_{crys})dm_{crys} \tag{9}$$

$$\frac{\partial f_{ice}(m_{crys})}{\partial t} = -\int f_{wat}(m_{drop})K(m_{crys}, m_{drop})f_{ice}(m_{crys})dm_{drop} + \int f_{wat}(m_{crys} - m_{crys}^*)K(m_{crys}^*, m_{crys} - m_{crys}^*)f_{ice}(m_{crys}^*)dm_{crys}^* \tag{10}$$

The collection efficiencies also follow Hall (1980). Table I shows the different hydrometeors collisions processes now considered in the DESCAM detailed microphysics scheme.

Due to turbulent diffusion process and/or updrafts motions a mixed-phase hydrometeor, *i.e.* an ice particle with a nonzero water ice ratio (WIR), can penetrates into the region of sub-zero temperatures. In that case the remaining ice core within the particle initiates the freezing of the surrounding meltwater coating. According to the local temperature and humidity conditions, the particle freezes inwards (Johnson and Hallett, 1968) until it is completely frozen into ice crystal. In order to consider the non-instantaneous freezing of the melting ice particles in the freezing levels the WIR is not immediately set to zero at the 0ºC isotherm level. As no lot of information is available about the freezing of the melting ice particles in the literature, a simple freezing parameterization is proposed. This parameterization considers the same approach than the non-instantaneous melting process (described by Eq. (1)) and assumes that the environmental temperature of freezing depends on the liquid water proportion of the melting particle. Thériault and Stewart (2010) consider a similar approach. Figure 5 illustrates the assumed functional dependency of the temperature of freezing T_{limit} for varying liquid proportions. This figure shows that the higher the liquid portion, the lower the temperature required for instantaneous complete re-freezing. However, the assumed threshold for the freezing temperature of the melting ice particles will probably depend on the cloud systems (convective or stratiform) and observations will be necessary to estimate it.

2.2. Elementary radar backscattering scheme

Olson *et al.* (2001) and Fabry and Szyrmer (1999) tested different methods for describing the dielectric properties of the mixed-phase particles. However, these different methods consider the melting particles as spongy particles with ice, liquid and air inclusions. As the DESCAM microphysics model used hereafter does not consider spongy hydrometeors with inclusions, a simpler backscattering scheme is needed. Thus, an elementary dielectric model is used below assuming that the radar backscattering of the wet ice particles are similar to those obtained from liquid drops of the same size. Indeed, this approach considers that the thin water layer insulates the ice core against the electromagnetic radiation of the weather radar, like a Faraday cage. In general, the radar reflectivity factor Z_l for liquid hydrometeors is calculated by taking into account the sixth moment of the simulated raindrop size distribution as given by Eq. (11):

$$Z_l[mm^6 m^{-3}] = \int N(D) D^6 dD \qquad (11)$$

In order to obtain the radar reflectivity factor of the mixed-phase particles Z_m, the used approach is the same than for the liquid hydrometeors considering the Eq. (11) where D is in that case the size of the wet ice particles D_m. For the ice phase, the approach of Delanoë *et al.* (2005) that provides the equivalent radar reflectivity factor Ze_i according to Eq. (12) is used:

$$Ze_i[mm^6 m^{-3}] = \frac{|K_i|^2}{|K_w|^2}\left(\frac{\rho_w}{\rho_i}\right)^2 \int N(D_{eq}) D_{eq}^6 dD_{eq} \tag{12}$$

The ice and water dielectrical constants are $|K_i|^2 = 0.176$ and $|K_w|^2 = 0.93$, respectively, for the usual meteorological radar wavelengths and D_{eq} is the equivalent diameter which corresponds to the diameter of a crystal after it completely melts. The equivalent diameter is given by:

$$D_{eq} = \left(\frac{\rho_i(D_i)}{\rho_w}\right)^{\frac{1}{3}} D_i \tag{13}$$

This approach is based on the Rayleigh approximation ($D < \frac{\lambda}{16}$; Doviac and Zrnić, 1984) considered for weather radars such as S or C band radars. Mie theory should be used for radars with smaller wavelengths (*e.g.* K band radars).

During the non-instantaneous melting process where the ice mass of the ice crystals is gradually converted into liquid mass, the size of the wet ice crystals is adjusted according to their water ice proportion. So, the electromagnetic properties of the melting hydrometeors present near the 0°C isotherm layer are linked to their water ice ratio.

3. Model setup

In order to test the new version of the DESCAM 3D detailed microphysics scheme which considers mixed phase hydrometeors, an idealised situation with a simple orography is modelled. This idealised case is similar to the one described by Zängl *et al.* (2010). The simulations have been performed on a single model domain with 202 × 98 grid points (150 × 72 km^2) and a horizontal grid spacing of 750 m. In the vertical, 83 model layers with an increment of about 40 m near the ground to about 600 m near the upper boundary (20 km) are used. Figure 6 shows the vertical grid spacing with height including a zoom onto the two first kilometres.

The topography is composed of an isolated bell-shaped mountain and a gentle slope situated in the lee side of the peak (see shaded area in Figure 7). The isolated mountain with the shape function, given by Eq. (14),

$$h(x,y)=\frac{h_0}{(1+\left(\frac{x}{L_x}\right)^2+(\frac{y}{L_y})^2)^2} \tag{14}$$

is located at x = 48 km and y = 36 km. The mountain height h_0 is equal to 1330 m, while the along-flow width scale L_x is 4 km and $L_y = 1.25\ L_x$. Around the bell-shaped mountain, the isolated mountain peak permits the formation of a gravity-wave which facilitates cloud system development. The slope is equal to +0.67% along the x-axis. This means that the topography increases 5 m in each subsequent x grid point. The slope begins at x = 30 km and at the lateral boundary (x = 150 km), its maximum altitude is 810 m. This slope permits the decrease of the intensity of the vertical motions. The use of this idealised topography is motivated by the fact that it forces the development of stratiform systems which are convenient for the study of the radar bright bands often visible in this type of situations.

The prescribed wind field is unidirectional along the x-direction with a speed U increasing from 10 m s^{-1} at the ground to 30 m s^{-1} at z = 11 km and remaining constant above. The Coriolis parameter is set to zero in all simulations. Thermodynamic sounding of the prescribed atmospheric conditions is provided by the winter case of Zängl *et al.* (2010). The initial aerosol particles distribution corresponds to the continental air mass used by Planche *et al.* (2010). The total number of aerosol particles in the boundary layer is 1411 cm^{-3} and the particles are assumed to be ammonium sulphate, 40% soluble (Brooks *et al.*, 2002) and with a molecular weight of 132 g mol^{-1}. The aerosol particle concentration decreases exponentially up to 3 km and is kept constant above.

The boundary conditions of the model assume free-slip conditions for the momentum components and zero normal second derivatives of all scalar variables at the upper and lower surface of the model. In order to prevent reflection of the vertically propagating gravity waves at the model top, a Rayleigh friction and Newtonian cooling absorber are employed in the uppermost region of the model. The lateral boundary conditions are approximated by open boundary conditions (Clark and Farley, 1984). The dynamical time step for the simulation is 3 s; however, the condensational growth needs significantly smaller time steps (Leroy, 2007).

4. Results and discussion

In this section, the influences of the new melting scheme on the microphysics, dynamics and thermodynamics properties of the idealised stratiform mixed phase cloud system are analysed. In the first paragraph, the general morphology of the cloud system is analysed for the old and the new melting scheme. A comparative study of the microphysics simulations using the instantaneous (I-) or the non-instantaneous (NI-) melting scheme is then developed. Lastly the impact of the mixed phase hydrometeors on the radar reflectivity is shown.

4.1. Cloud system morphology

In both simulations, the macroscopic development and aspect of the cloud system are quite similar. Indeed, during the 30 first minutes, the isolated mountain induces the formation of a gravity-wave which modifies the wind field. Updrafts and downdrafts appear at the windward and leeward sides of the mountain. The vertical motions are present up to 6 km height and their maximum intensity is approximately 4 m s^{-1}. The association of the updraft patterns and the environmental humidity and temperature conditions permits the formation of a liquid phase cloud system at the summit of the mountain. As expected a stratiform cloud system forms at the lee side of the mountain over the gentle slope (Figure 7). The ice phase appears after approximately 1 hour of integration in the sub-zero temperature areas and reaches a maximum of 0.4 g cm^{-3} at 150 min of integration. Each simulation lasts 4 hours.

4.2. Comparison of the time dependent and the instantaneous melting process

4.2.1. Microphysics influence

The simulation results obtained with the I-melting scheme (instantaneous) are compared with the ones of the NI-simulations (non-instantaneous). In a first step, the analysis focuses on the liquid and ice phase fields. Figure 7 shows the liquid water content (LWC) and the ice water content (IWC) after 150 min of integration obtained with the I- and the NI-melting process. The LWC and IWC include the cloud and precipitating mass of each water phase. Hereafter, the modelling results are always presented at 150 min of integration because the ice phase is abundant at this time.

According to the Figures 7(a) and (c), the repartition of the IWC is quite similar regardless the used melting process. In fact, the IWC is mainly present far behind the leeward side of the isolated mountain with a maximum amount of 0.4 g m^{-3} at x = 130 km. Nevertheless, in the NI-case, the ice phase exists in area with positive temperatures whereas it suddenly disappears at the 0^{o}C isotherm altitude in the I-case. Figure 7(a) shows that the melting layer has a depth of approximately 200 m in the NI-case. The maximum amounts (1.5 g m^{-3}) of the LWC are similar in the two simulations. Nevertheless, the repartition of the LWC is quite different below the melting layer. In the I-melting case, the maximum amount of the LWC is located just below the 0^{o}C isotherm level. In contrast, in the NI-case, there is no abrupt increase of the LWC just below the 0^{o}C level, but a gradual increase of the LWC exists below the 0^{o}C isotherm level until a maximum at approximately 1 km altitude height. This behaviour has also been reported by Phillips *et al.* (2007) and results from the continuous melting of the ice phase that is progressively transferred into the liquid phase. Figures 7(b) and (d) also include the rain field. In both cases, the precipitation is mainly caused by melting of the ice phase. The rain quantity is similar in both simulations except near the 0ºC isotherm level. The precipitation forms in lower levels of the atmosphere in the NI-case than in the I-case. In fact, the liquid phase becomes available at lower altitudes in the NI-case where the collision-coalescence process, which forms larger drop sizes, becomes effective. However, the implementation of the non-instantaneous melting process does not modify the features of the cumulative rain field since its repartition is the same and its maximum amount situated in the lee side of the mountain remains equal to 3.12 mm after 150 min of integration (not shown).

Figure 8 shows the ice and liquid mass spectra for the two simulations (with the I- or the NI-melting process) after 150 min of integration and, at different altitudes averaged over 5 × 5 km^2 areas (49 grid points) whose each centres are represented by the black "plus" symbols in the Figure 7(a). The three different altitudes to study the hydrometeors mass spectra have been selected above, below and inside the melting layer. At this *x* position, the 0^{o}C isotherm altitude is approximately at 1200 m. For the I-melting case, the Figures 8(c) and (d) show that the ice crystal mass is suddenly transferred into the liquid mass content at the 0^{o}C isotherm level. Here, the I-melting of the large precipitating ice crystals permits the formation of large raindrops. Below the 0^{o}C isotherm level, the liquid mass varies with the altitudes. This variation is due to the collision-coalescence and evaporation processes which are efficient in the positive temperature areas. Figures 8(a) and (b) show the ice[1] and liquid mass spectra obtained with the NI-melting process. The ice phase is now present below the 0^{o}C isotherm level. However, the ice mass content decreases with the increasing temperature due to the NI-melting process. An increase of the liquid phase is associated with this decrease in the ice

---

[1] Note that a change in diameter size from the ice crystal spectra of Figure 8(a) and (c) to the droplet spectra given in Figure 8(b) and (d) remains quite weak, as we consider a spherical form of the crystals and an ice density of 0.9 g cm^{-3}. The liquid and glaciated diameter of the same hydrometeor mass bin thus differs by 3.5% only.

mass. The two maxima of the water drop distribution represent the two liquid-types particles those are the cloud droplets and the raindrops. In the opposite, the ice mass distribution have only one maximum since at these levels only the precipitating ice particles are present while the cloud ice particles are located at higher altitudes. Figure 9 shows the evolution of the WIR parameter according to the altitudes. The crystals that are melting are represented by the different colour areas. The blue ones represent the ice crystals with low meltwater amounts whereas the red ones represent the ice crystals with high meltwater amounts. Figure 9 shows that the small crystals melt faster than the larger ones. We can also see that, below the 0°C isotherm level, the WIR is varying according to either the local thermodynamics conditions and/or the collisions between hydrometeors which modify the water-ice proportion of the new formed particles. For example, the collisions between drop and wetted ice crystal form mixed-phase hydrometeor with more important water proportion. In the opposite, the aggregation process forms wetted ice crystals with less important water proportion. Figure 9 also shows that some melting ice crystals are present above the 0°C isotherm level. Among other hydrometeors, the wetted ice crystals are advected into the sub-zero temperature areas due to the turbulence and the vertical wind speeds existing in the system. As the environmental temperature of freezing is assumed to be dependent on the liquid (or ice) water proportion of the particle (Section 2.1), the wetted ice crystals do not freeze instantaneously at 0°C. For example, for the different diameters of wetted ice crystals existing at 630 m agl, the WIRs are ranged between 0.18 and 0.73, i.e. the ice proportion is ranged between 27% and 82%. As the surrounding environmental temperature is equal to -0.14°C at this time and altitude, the ice proportion seems to be too few in order to trigger the freezing of the wetted ice crystals (see Figure 5). Microphysically, the higher the ice proportion, the faster the rate of refreezing of the wetted ice crystals. Figure 9 also shows that, as expected, the smallest ice particles melt quicker than the larger ones. This comparative study demonstrates the correct functioning of the microphysics behaviour of the new NI-melting process.

4.2.2. Thermodynamic and dynamics influence

The impact of the new microphysics representation on the released or absorbed latent heat associated with the phase change processes associated to the ice crystal melting and/or the riming of the droplets are now analysed. From Figure 7 it becomes obvious that inside the stratiform precipitation region the isotherm 0°C lines do not follow the same horizontal pattern as the isotherm lines for 2, -2 and -4°C. We can suppose that this deviation is affected by the thermodynamics of the melting processes. Figure 10 shows the difference between the environmental temperatures obtained with the I-melting scheme and with the NI-melting scheme after 150 min of integration. The red contours show the vertical regions wherein temperatures remain warmer in the NI-scheme; the blue contours those where the NI-scheme results in more cooling than the I-scheme. This figure also shows that the 0°C isotherm behaves different for the I- and NI- melting scheme: the solid line gives the 0°C line for the NI-scheme, while the dashed line the one for the I-scheme. The 0°C isotherm level of the I-case appears about 100 m lower than in the NI-case. The latent heat associated with the melting process modifies the temperature field. The consumed latent heat during this microphysical process is proportional to the melted ice mass. At the 0°C isotherm level, the melted ice mass and, then, the consumed latent heat are more important in the I-case. Thus, this consumption induces colder environment temperatures in the I-melting scheme and forces the 0°C line to lower levels. The NI- time dependent melting scheme, however, transforms less ice to water next to the 0°C level but the melting process remains still efficient at lower altitudes by producing latent cooling down to 200 m below the 0°C isotherm level. The associated latent heat evolutions with the continuous melting process better represent the actual thermodynamic behaviours.

In addition, the changes in the latent heat fields modify the vertical wind properties. The vertical motions seem to be slightly intensified by the temperature changes. In fact, the change of +0.25 ºC in the temperature field increases the updraft wind of approximately 10 cm s^{-1} (not illustrated). This change is quite weak in this stratiform situation but Phillips *et al.* (2007) showed that the consumed latent heat during the melting process in a deep convective cloud could induce a different dynamical evolution of the cloud system.

4.3. Bright band representation

The impact of the mixed phase hydrometeors on the radar reflectivity characteristics is evaluated in this section, in particular, whether the DESCAM microphysics scheme is now able to reproduce the radar bright band phenomenon as other bulk schemes (e.g. Morrison *et al.*, 2009). Figure 11 shows the temporal evolution of the vertical profile of the radar reflectivity obtained at x = 130 km and y = 36 km for the I- and the NI-case. This position corresponds to the location where the ice phase content and the cumulative rain amount at the ground are abundant. Figure 11 shows that precipitation starts at around 5000 s (≈ 84 min) in both cases. In the NI-case (Figure11b), the radar bright band appears at 6000 s (100 min) at approximately 600 m above ground level (agl) whereas at the same altitude in the I-case (Figure11a) a change characterizing the different water phases of the hydrometeors (ice crystals or drops) is visible in the reflectivity field. Indeed, in this case, the simulated radar reflectivity for the ice crystals is approximately $Z_i < 10$ dBZ whereas the radar reflectivity can reaches 18 dBZ for the rain. In the NI-case, the maximum of the radar reflectivity located in the radar bright band is 20 dBZ and remains constant all along the simulation. Above and below the radar bright band, the radar reflectivities are decreasing due to the smaller dielectric constant of the dry ice crystals and the smaller sizes of drops compared to the ones of the wetted ice crystals. The radar reflectivity values increase close to the surface (between 300 m agl and ground) because the collision-coalescence process, which becomes more effective, produces larger drops. This process is more visible in the I-case where the drop sizes are slightly larger since they are available at higher altitudes than in the NI-case. The model capacity to reproduce the bright band will complement the radar measurements in order to resolve the complex microphysics near the 0ºC level of the atmosphere, and will help to reduce the important uncertainties in the precipitation estimation at the ground associated with this phenomenon.

5. Summary and conclusions

In this study, a new non-instantaneous melting scheme which considers mixed-phase hydrometeors is implemented in the DESCAM-3D detailed microphysics scheme. According to the theory of Mason (1956) and the lab experiments of Rasmussen and Pruppacher (1982), two parameterisations are developed to characterize the temperature at which the melting process starts and the melting rate of the ice particles. These parameterisations are mainly dependent of the environmental parameters: humidity and temperature and also the mass of the ice crystals. In order to consider the mixed-phase hydrometeors, a new distribution discretized into 30 bins is added considering the water ice mass ratio of each melting ice particles. Furthermore, the aggregation process which is more efficient in the melting level due to the meltwater thin layer present around the ice particle, and the collisions between melting ice particles and drops present below the 0ºC isotherm height are now treated in the detailed microphysics scheme. A freezing parameterization was also developed to consider the freezing of the advected melting ice particles in sub-zero temperature area. This parameterization assumes that the freezing of mixed-phase particles is easier when the ice proportion is bigger.

The new version of the melting scheme is tested in an idealised simulation case. The idealised topography is composed of an isolated mountain and a gentle slope situated in its lee-side and permits to obtain a mixed phase stratiform system where the radar bright band phenomena are often visible. This study shows that the new melting scheme does not modify the macrophysics properties of this slow dynamics system. However, it changes the microphysics and thermodynamics properties. In fact, the ice particles are enabled to fall in lower levels where the atmospheric temperatures are greater than 0 ºC. Moreover, the phase change associated with the melting process produces slight latent cooling just below the 0ºC isotherm level that can influence the dynamics of the system. This effect should be more prominent in deep convective cases where the dynamics motions are more intense than in this stratiform situation (Phillips *et al.*, 2007). The different analyses show that the new melting scheme produces satisfactory results.

The implementation of the continuous melting process in association with a backscattering scheme permits to reproduce the radar bright band phenomenon which is well known to induce uncertainties in the precipitation estimation. As the microphysics scheme only consider one type of non-spongy ice particles, an elementary backscattering scheme assimilating the melting ice particles to drops is implemented. However, as indicated by the latest studies led by Olson *et al.* (2001), the intensity of the radar bright band is strongly dependent on the density of the melting ice crystal and on the considered representation of the ice particle, i.e. water and air inclusions in the ice core. As a consequence, in the future, it is planned to develop a more realistic freezing parameterisation relying observations and comparative studies and test the new melting scheme in real stratiform and convective cases to understand the impact of this process on the cloud system lifetime and dynamics considering different ice morphologies to better reproduce the bright band phenomena and then assist the radar users to reduce the uncertainties in the precipitation estimation at the ground.

Acknowledgement

The lead author would like to thank the anonymous reviewers for their precise and constructive comments which have significantly contributed to the improvement of the article. The calculations for this study have been done on computer facilities of the Institut du Développement des ressources en Informatique Scientifique (IDRIS), CNRS at Orsay and the Centre Informatique National de l’Enseignement Supérieur (CINES) at Montpellier under the project 940180. The authors acknowledge with gratitude the hours of computer time and the support provided.

References

Barth MC, Parsons DB. 1996. Microphysical processes associated with intense frontal rainbands and the effect of evaporation and melting on frontal dynamics. *J. Atmos. Sci.* 53: 1569-1586.

Battan LJ. 1973. *Radar Observation of the Atmosphere*. University of Chicago Press: Chicago; pp 324.

Bohren CF, Battan LJ. 1982. Radar backscattering of microwaves by spongy ice spheres. *J. Atmos. Sci.* 39: 2623-2628.

Bott A. 1998. A flux method for the numerical solution of the stochastic collection equation. *J. Atmos. Sci.* 55: 2284-2293.

Brooks SD, Wise ME, Cushing M, Tolbert MA. 2002. Deliquescence behavior of organic/ammonium sulfate aerosol. *Geophys. Res. Lett.* 29: 1917. DOI: 10.1029/2002GL014733.

Clark TL, Hall WD. 1991. Multi-domain simulations of the time dependent Navier-Stokes equations: benchmark error analysis of some nesting procedure. *J. Comp. Phys.* 92: 456-481.

Clark TL, Farley RD. 1984. Severe downslope windstorm calculations in two and three spatial dimensions using anelastic interactive grid nesting: a possible mechanism for gustiness. *J. Atmos. Sci.* 41: 329–350.

Delanoë J, Protat A, Testud J, Bourniol B, Heymsfield AJ, Bansemer A, Brown PRA, Forbes M. 2005. Statistical properties of the normalized ice particle size distribution. *J. Geophys. Res*. 110: D10201. DOI: 10.1029/2004JD005405.

Doviac RJ, Zrnić DS. 1984. *Doppler radar and weather observations*. Academic Press; pp 458.

Fabry F, Zawadzki I. 1995. Long-term radar observations of the melting layer of precipitation and their interpretation. *J. Atmos. Sci.* 52: 838-851.

Fabry F, Szyrmer W. 1999. Modeling of the melting layer. Part II: Electromagnetic. *J. Atmos. Sci.* 56: 3593-3600.

Ferrier BS. 1994. A double-moment multiple-phase four-class bulk ice scheme. Part I: Description. *J. Atmos. Sci.* 51: 249–280.

Flossmann AI, Hall WD, Prupaccher HR. 1985. A theoretical study of the wet removal of atmospheric pollutants. Part I: the redistribution of aerosol particles captured through nucleation and impaction scavenging by growing cloud drops. *J. Atmos. Sci.* 42: 582–606.

Flossmann AI, Wobrock W. 2010. A review of our understanding of the aerosol-cloud interaction from the perspective of a bin resolved cloud scale modeling. *Atmos. Res.* 97: 478-497. DOI: 10.1016/j.atmosres.2010.05.008.

Fridlind AM, Ackerman AS, Jensen EJ, Heymsfield AJ, Poellot MR, Stevens DE, Wang D, Miloshevich LM, Baumgardner D, Lawson RP, Wilson JC, Flagan RC, Seinfeld JH, Jonsson HH, VanReken TM, Varutbangkul V, Rissman TA. 2004. Evidence for the predominance of mid-tropospheric aerosol as subtropical anvil cloud nuclei. *Science*. 304: 718-722. DOI: 10.1126/science.1094947.

Hall WD. 1980. A detailed microphysical model within a two-dimensional dynamic framework: model description and preliminary results. *J. Atmos. Sci.* 37: 2486-2507.

Hardaker PJ, Holt AR, Collier CG. 1995. A melting-layer model and its use in correcting for the bright band in single-polarization radar echoes. *Quart. J. Roy. Meteor. Soc.* 121: 495-525. DOI: 10.1002/qj.49712152303.

Heymsfield AJ, Iaquinta J. 2000. Crystal terminal velocities. *J. Atmos. Sci.* 57: 916–938.

Heymsfield AJ, Pflaum JC. 1985. A quantitative assessment of the accuracy of techniques for calculating graupel growth. *J. Atmos. Sci.* 42: 2264–2274.

Johnson DA, Hallett J. Freezing and shattering of the supercooled water drops. *Quart. J. Roy. Meteorol. Soc.* 402: 468-482.

Joss J, Waldvogel A. 1990. *Precipitation measurement and hydrology, Radar in Meteorology*. D. Atlas Ed., Amer. Meteor. Soc.; pp 577-597.

Klaassen W. 1988. Radar observations and simulation of the melting layer of precipitation. *J. Atmos. Sci.* 45: 3741-3753.

Koop THP, Luo B, Tsias A, Peter T. 2000. Water activity as the determinant for homogeneous ice nucleation in aqueous solutions. *Nature*. 406: 611–615.

Leroy D. 2007. Développement d'un modèle de nuage tridimensionnel a microphysique détaillée – Application à la simulation de cas de convection moyenne et profonde. PhD thesis, Blaise Pascal University, Clermont-Ferrand (France), pp 201. Available at http://wwwobs.univ-bpclermont.fr/atmos/fr/Theses/Th_Leroy.pdf

Liu C, Moncrieff MW, Zipser EJ. 1997. Dynamical influence of microphysics in tropical squall lines: A numerical study. *Mon. Wea. Rev*, 125: 2193–2210.

Lynn BH, Khain A, Dudhia J, Rosenfeld D, Pokrovsky A, Seifert A. 2005. Spectral (bin) microphysics coupled with a mesoscale model (MM5). Part I: Model description and first results. *Mon. Wea. Rev.* 133: 44-58. DOI: 10.1175/MWR-2840.1.

Mason BJ. 1956. On the melting of hailstones. *Quart. J. Roy. Meteorol. Soc.* 82: 209-216. DOI: 10.1002/qj.49708235207.

Maxwell-Garnett JC. 1904. Colors in metal glasses and in metallic films. *Philos. Trans. Roy. Soc. London.* 203A: 385-420.

Meneghini R, Liao L. 1996. Comparisons of cross sections for melting hydrometeors as derived from dielectric mixing formulas and a numerical model. *J. Appl. Meteor.* 35: 1658-1670.

Meyers MP, Demott PJ, Cotton WR. 1992. New primary ice nucleation parameterizations in an explicit cloud model. *J. Appl. Meteorol.* 31: 708–721.

Mitra SK, Vohl O, Ahr M, Pruppacher HR. 1990. A wind tunnel and theoretical study of the melting behavior of atmospheric ice particles. IV: Experiment and theory for snowflakes. *J. Atmos. Sci.* 47: 584-591.

Monier M, Wobrock W, Gayet JF, Flossmann AI. 2006. Development of a detailed microphysics cirrus model tracking aerosol particles histories for interpretation of the recent INCA campaign. *J. Atmos. Sci.* 63: 504–525.

Morrison H, Thompson G, Tatarskii V. 2009. Impact of cloud microphysics on the development of trailing stratiform precipitation in a simulated squall line: Comparison of one- and two-moment schemes. *Mon. Wea. Rev.* 137: 991-1007.

Olson WS, Bauer P, Viltard NF, Johnson DE, Tao W, Meneghini R, Liao L. 2001. A melting-layer model for passive/active microwave remote sensing applications. Part I: Model formulation and comparison with observations. *J. Appl. Meteor.* 40: 1145-1163.

Ovtchinnikov M, Kogan YL. 2000. An investigation of ice production mechanisms in small cumuliform clouds using a 3D model with explicit microphysics. Part I: Model description. *J. Atmos. Sci.* 57: 2989-3003.

Phillips VTJ, Pokrovsky A, Khain A. 2007. The influence of time-dependent melting on the dynamics and precipitation production in maritime and continental storm clouds. *J. Atmos. Sci.* 64: 338-358. DOI: 10.1175/JAS3832.1.

Planche C, Wobrock W, Flossmann AI, Tridon F, Van Baelen J, Pointin Y, Hagen M. 2010. The influence of aerosol particle number and hygroscopicity on the evolution of convective cloud systems and their precipitation: A numerical study based on the COPS observations on 12 August 2007. *Atmos. Res.* 98: 40-56. DOI: 10.1016/j.atmosres.2010.05.003.

Pruppacher HR, Klett JD. 1997. *Microphysics of clouds and precipitation*. 2^{nd} Ed. Kluwer Academic Publishers; pp 954.

Rasmussen RM, Heymsfield AJ. 1985. A generalized form for impact velocities used to determine graupel accretional densities. *J. Atmos. Sci.* 42: 2275–2279.

Rasmussen RM, Heymsfield A. 1987a. Melting and shedding of graupel and hail. Part I: Model Physics. *J. Atmos. Sci.* 44: 2754-2763.

Rasmussen RM, Heymsfield A. 1987b. Melting and shedding of graupel and hail. Part II: Sensitivity study. *J. Atmos. Sci.* 44: 2764-2782.

Rasmussen RM, Levizzani V, Pruppacher HR. 1984a. A wind tunnel and theoretical study of the melting behavior of atmospheric ice particles. II: A theoretical study for frozen drops of radius < 500 μm. *J. Atmos. Sci.* 41: 374–380.

Rasmussen RM, Levizzani V, Pruppacher HR. 1984b. A wind tunnel and theoretical study of the melting behavior of atmospheric ice particles. III: Experimental and theory for spherical ice particles of radius > 500 μm. *J. Atmos. Sci.* 41: 381–388.

Rasmussen RM, Pruppacher HR. 1982. A wind tunnel and theoretical study of the melting behavior of atmospheric ice particles. I: A wind tunnel study of the frozen drops of radius < 500 µm. *J. Atmos. Sci.* 39: 152-158.

Smith CJ. 1986. The reduction of errors caused by bright bands in quantitative rainfall measurements made using radar. *J. Atmos. Oceanic Technol.* 3: 129-141.

Szeto KK, Stewart RE, Lin CA. 1988. Mesoscale circulations forced by the melting of snow in the atmosphere. Part II: Application to meteorological features. *J. Atmos. Sci.* 45: 1642–1650.

Szyrmer W, Zawadzki I. 1999. Modeling of the melting layer. Part I: Dynamics and microphysics. *J. Atmos. Sci.* 56: 3573-3592.

Thériault JM, Stewart RE. 2010. A parameterization of the microphysical processes forming many types of winter precipitation. *J. Atmos. Sci*. 67: 1492-1508.

Wei Y, Marwitz J. 1996. The Front Range blizzard of 1990. Part III: Numerical simulations of melting effects. *Mon. Wea. Rev.* 124: 2483–2496.

Zängl G, Seifert A, Wobrock W. 2010. Modeling stable orographic precipitation at small scales: The impact of the autoconversion scheme. *Meteorol. Z.* 19: 405-416.

Table

Table I: Synthesis of the different hydrometeors collisions considered in the DESCAM-3D detailed microphysics scheme

	Drop	**ice particle**	**wetted ice particle**
Drop	Drop	ice particle *if* $T_e < 0^{o}C$	wetted ice particle *if* $WIR < 1$
		wetted ice particle *if* $T_e > 0^{o}C$	drop *if* $WIR \approx 1$
ice particle	ice particle *if* $T_e < 0^{o}C$	ice particle	wetted ice particle
	wetted ice particle *if* $T_e > 0^{o}C$		
wetted ice particle	wetted ice particle *if* $WIR < 1$	wetted ice particle	wetted ice particle
	drop *if* $WIR \approx 1$		

Figures

Figure 1: Melting process according to the theory of Mason (1956) at the time *t*.

Figure 2: Parameterization as a function of relative humidity and temperature of the air at which an ice sphere does/does not melt due to evaporative cooling at the ice-sphere surface. Comparison with theory of Mason (1956) and the lab experiment of Rasmussen and Pruppacher (1982). Adapted from Rasmussen and Pruppacher (1982).

Figure 3: Schematic representation of the melting process in the DESCAM model. When the WIR parameter of the ice particle > 10 µm, is equal to 1 the completely melted ice particles are transferred to the drop reservoir. This transfer corresponds to the arrows. To simplify the diagram, only some of the 30 bins which are common to the ice particle, drop and ice water ratio grids are represented.

Figure 4: Radius of the ice core of a melting ice sphere of 350 µm as a function of time, for various warming rates, obtained by Rasmussen and Pruppacher (1982) and with the melting rate parameterisation of Eq. (4). Adapted from Rasmussen and Pruppacher (1982).

Figure 5: Parameterization as a function of temperature and water ice ratio at which the melted ice particle does/does not freeze.

Figure 6: Variation of the vertical grid spacing of the domain. The small panel shows a zoom on the 2 lowest kilometres.

Figure 7: Vertical cross sections of the Ice Water Content (IWC) in g m^{-3} (a,c) and the Liquid Water Content (LWC) in g m^{-3} (b,d) obtained with the non-instantaneous (a,b) and the instantaneous melting scheme (c,d) after 150 min of integration. The black lines represent the isotherms (in ºC). The grey lines show the rain content (in g kg^{-1}). The “plus” symbols characterise the different altitudes considered in the Figure 8.

Figure 8: Mean mass spectra of the ice crystals (a,c) and of the drops (b,d) obtained with the non-instantaneous (a,b) and the instantaneous (c,d) melting scheme at different altitudes. The hydrometeors mass spectra are averaged over a 5 × 5 km^2 areas (49 grid points) whose centres are represented by a “plus” symbols in Figure 7. The three chosen altitudes represent the hydrometeors mass spectra above (1400 m height, solid lines), below (1080 m height, dotted lines) and inside the melting layer (1200 m, dashed lines). The grey area corresponds to the precipitating hydrometeors in DESCAM 3D.

Figure 9: Evolution of the Water Ice Ratio (WIR) distribution according to the altitudes at 150 min of integration and at the same point than Figures 7 and 8. WIR equal to 0 or 1 represent crystals or drop, respectively. The empty ice size bins are not shown. The black continuous line represents the altitude of the 0°C isotherm.

Figure 10: Vertical cross section of the temperature difference between the NI- and the I-melting simulations obtained after 150 min of integration at y = 48 km. The blue contours correspond to the colder regions in the NI-simulation whereas the red contours show warmer region in the NI-simulations. The continuous and dashed black lines represent the isotherms in °C in the NI- and I- simulation cases, respectively.

Figure 11: Temporal evolution of the vertical profile of the radar reflectivity over the position x = 130 km and y = 36 km obtained with the instantaneous (a) and the non-instantaneous (b) melting process.

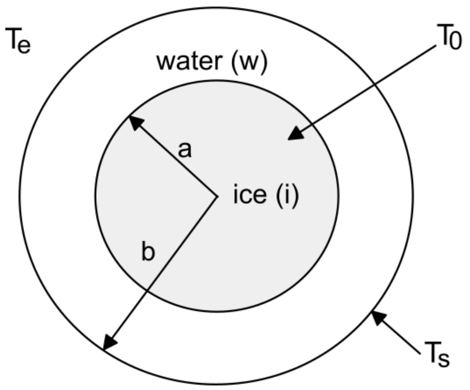

Figure 1

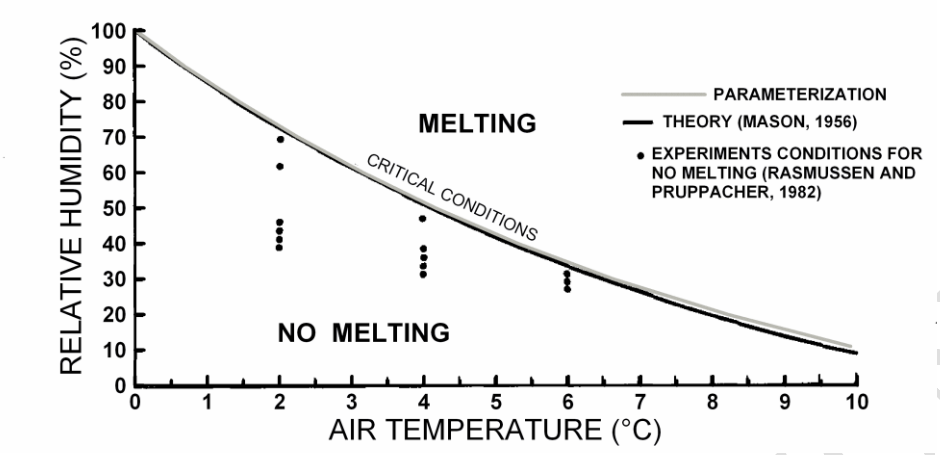
RELATIVE HUMIDITY (%)
100
90
80
70
60
50
40
30
20
10
0
MELTING
CRITICAL CONDITIONS
NO MELTING
PARAMETERIZATION
THEORY (MASON, 1956)
EXPERIMENTS CONDITIONS FOR NO MELTING (RASMUSSEN AND PRUPPACHER, 1982)
0
1
2
3
4
5
6
7
8
9
10
AIR TEMPERATURE (°C)

Figure 2

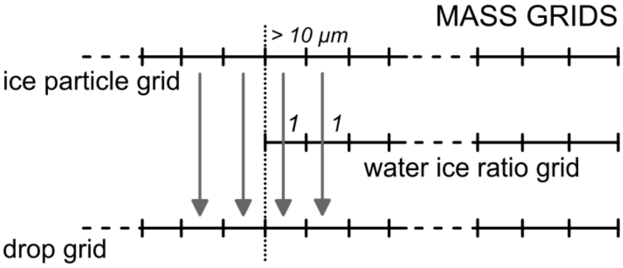
MASS GRIDS
> 10 μm
ice particle grid
1
1
water ice ratio grid
drop grid

Figure 3

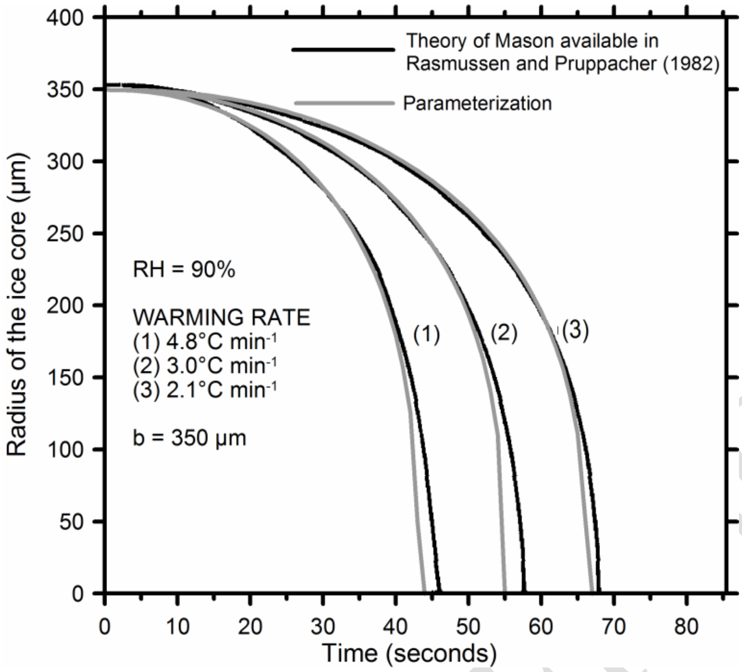
Theory of Mason available in Rasmussen and Pruppacher (1982)
Parameterization
RH = 90%
WARMING RATE
(1) 4.8°C min^{-1}
(2) 3.0°C min^{-1}
(3) 2.1°C min^{-1}
b = 350 µm
(1)
(2)
(3)
Radius of the ice core (µm)
400
350
300
250
200
150
100
50
0
Time (seconds)
0
10
20
30
40
50
60
70
80

Figure 4

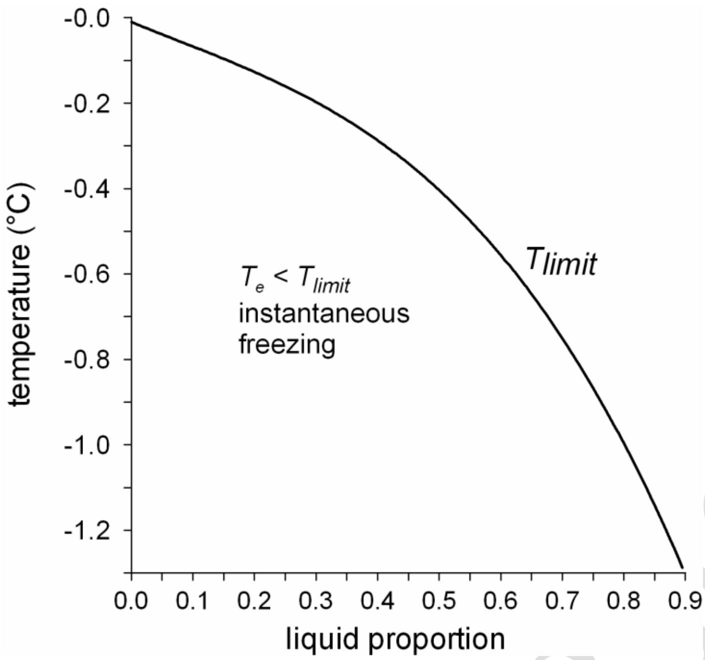
-0.0
-0.2
-0.4
-0.6
-0.8
-1.0
-1.2
temperature (°C)
T_{limit}
$T_e < T_{limit}$
instantaneous
freezing
0.0
0.1
0.2
0.3
0.4
0.5
0.6
0.7
0.8
0.9
liquid proportion

Figure 5

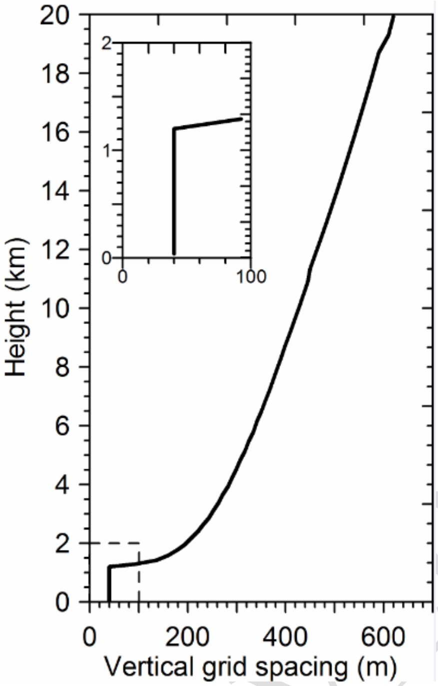

20
18
16
14
12
10
8
6
4
2
0
Height (km)
0
200
400
600
Vertical grid spacing (m)
2
1
0
0
100

Figure 6

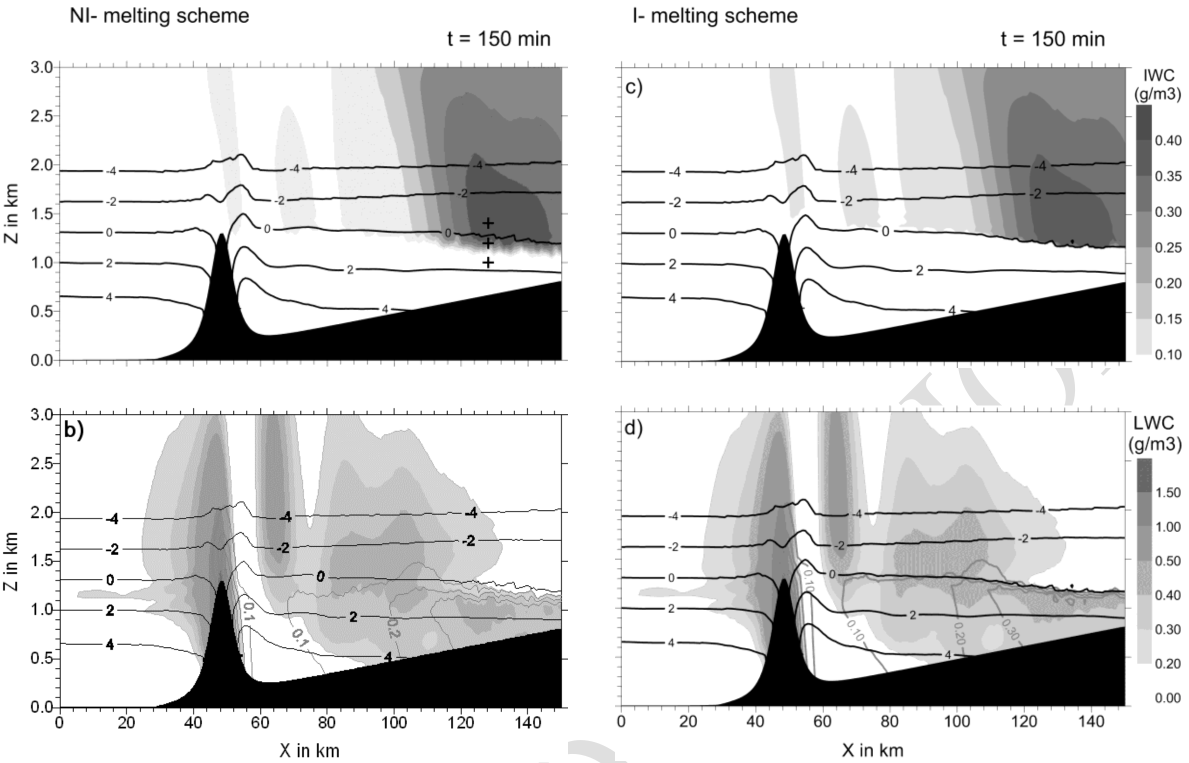
NI- melting scheme
t = 150 min
I- melting scheme
t = 150 min
c)
b)
d)
IWC
(g/m3)
0.40
0.35
0.30
0.25
0.20
0.15
0.10
LWC
(g/m3)
1.50
1.00
0.50
0.40
0.30
0.20
0.00
Z in km
X in km
3.0
2.5
2.0
1.5
1.0
0.5
0.0
0
20
40
60
80
100
120
140
-4
-2
0
2
4
0.1
0.2
0.10
0.20
0.30

Figure 7

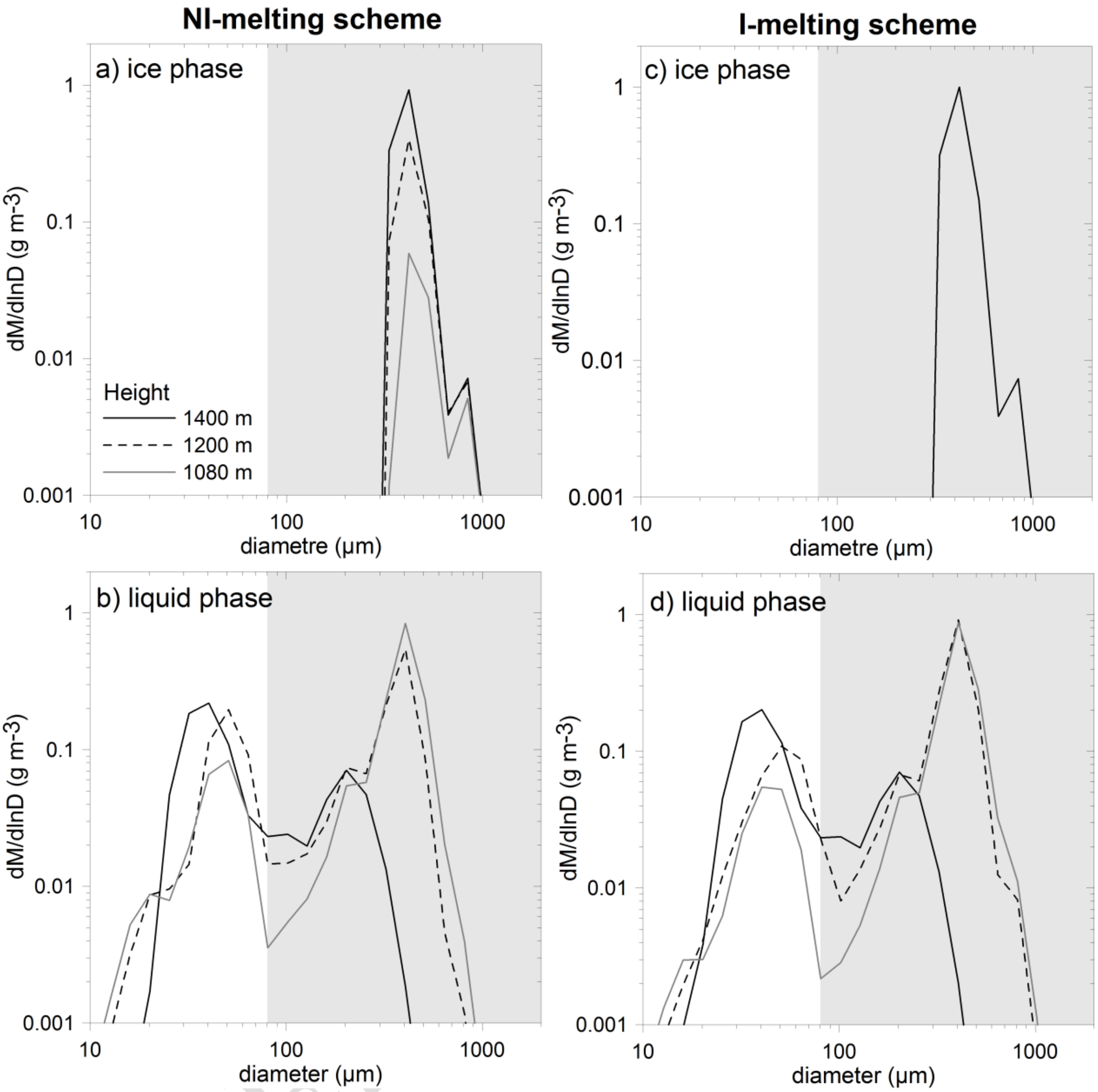
NI-melting scheme
I-melting scheme
a) ice phase
b) liquid phase
c) ice phase
d) liquid phase
dM/dlnD (g m-3)
0.001
0.01
0.1
1
10
100
1000
diametre (µm)
diameter (µm)
Height
1400 m
1200 m
1080 m

Figure 8

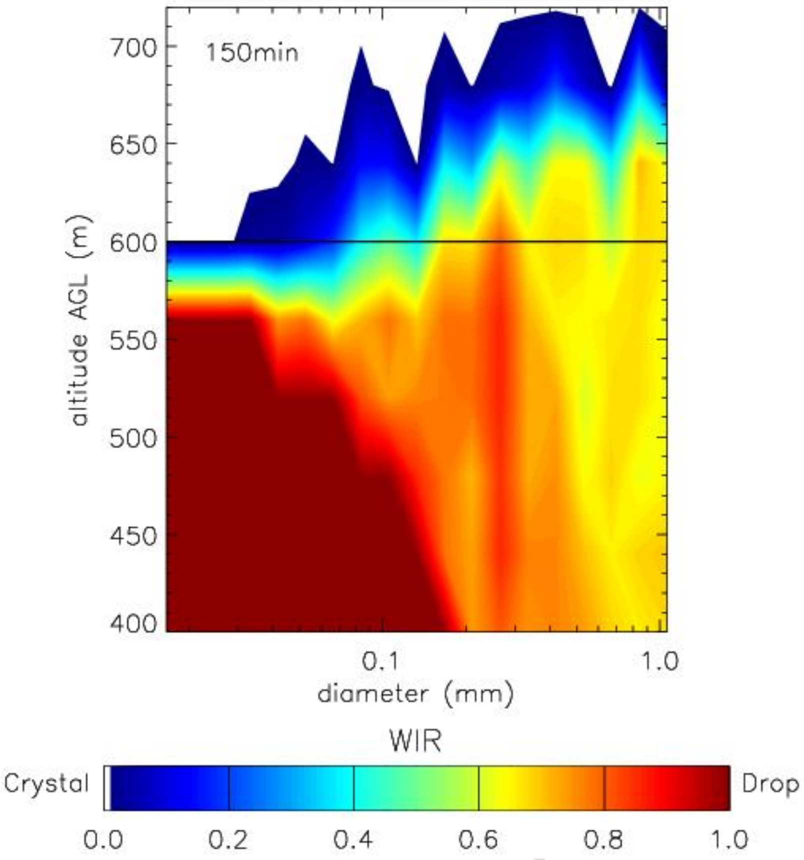
150min
altitude AGL (m)
700
650
600
550
500
450
400
0.1
1.0
diameter (mm)
WIR
Crystal
Drop
0.0
0.2
0.4
0.6
0.8
1.0

Figure 9

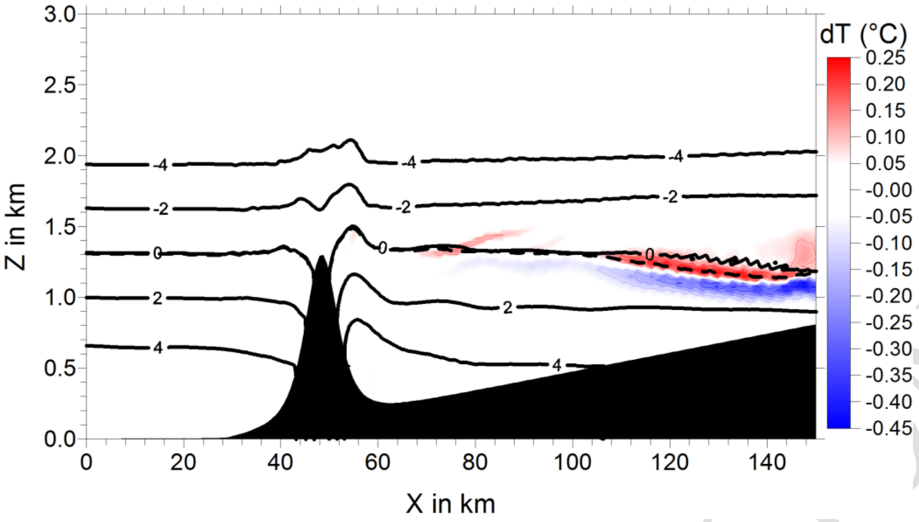
Z in km
3.0
2.5
2.0
1.5
1.0
0.5
0.0
X in km
0
20
40
60
80
100
120
140
-4
-2
0
2
4
dT (°C)
0.25
0.20
0.15
0.10
0.05
-0.00
-0.05
-0.10
-0.15
-0.20
-0.25
-0.30
-0.35
-0.40
-0.45

Figure 10

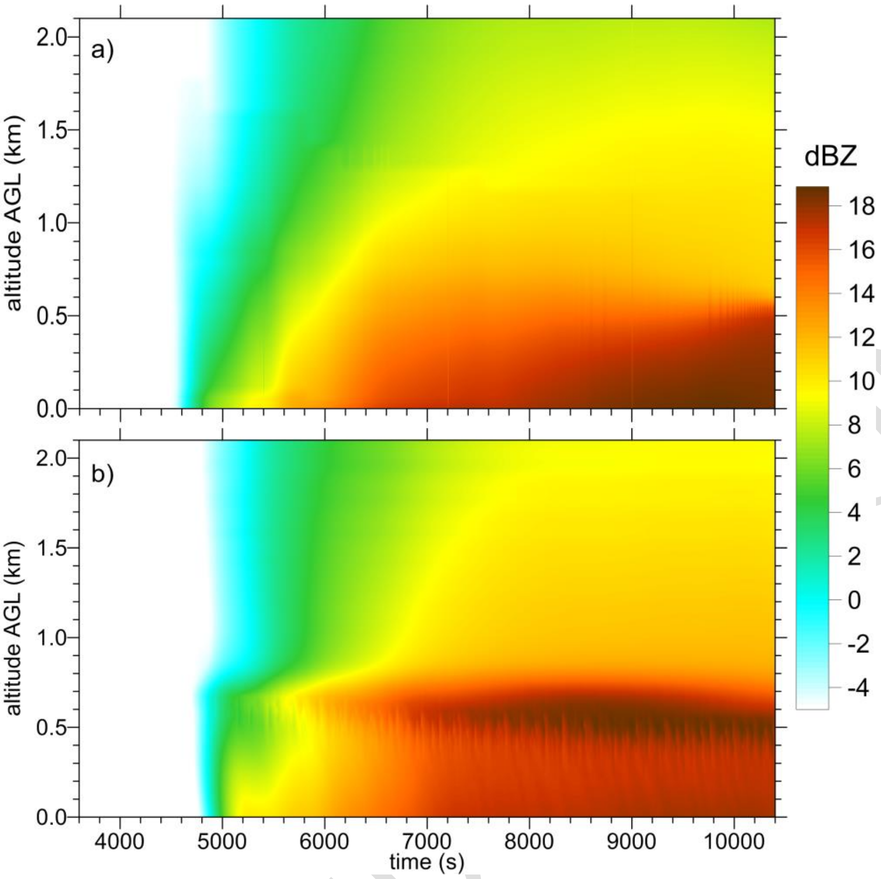
a)
b)
altitude AGL (km)
0.0
0.5
1.0
1.5
2.0
dBZ
18
16
14
12
10
8
6
4
2
0
-2
-4
4000
5000
6000
7000
8000
9000
10000
time (s)

Figure 11